frontiers | Frontiers in Earth Science

TYPE Original Research
PUBLISHED 16 January 2023
DOI 10.3389/feart.2022.1074178

OPEN ACCESS

EDITED BY
Ali Abedini,
Urmia University, Iran

REVIEWED BY
Akram Alizadeh,
Urmia University, Iran
Zhifu Wei,
Institute of Geology and Geophysics (CAS), China

*CORRESPONDENCE
Lamei Lin,
linlameiupc@upc.edu.cn

SPECIALTY SECTION
This article was submitted to Geochemistry, a section of the journal Frontiers in Earth Science

RECEIVED 19 October 2022
ACCEPTED 22 November 2022
PUBLISHED 16 January 2023

CITATION
Lin L, Cheng F and Xu J (2023), Preservation of molecular fossils in carbonate concretions in cretaceous shales in the songliao basin, northeast China.
Front. Earth Sci. 10:1074178.
doi: 10.3389/feart.2022.1074178

Preservation of molecular fossils in carbonate concretions in cretaceous shales in the songliao basin, northeast China

Lamei Lin[1,2]*, Fuqi Cheng[1,2] and Jinjun Xu[1,2]

[1]School of Geosciences, China University of Petroleum, Qingdao, Shandong, China, [2]Shandong Provincial Key Laboratory of Deep Oil & Gas, China University of Petroleum, Qingdao, Shandong, China

Paleoenvironmental information is better preserved in carbonate concretions. In this study, carbonate concretions in the Cretaceous Nenjiang shale, Songliao Basin, were examined to determine whether molecular fossils reflective of the paleoenvironment were better preserved at these sites. Organic and inorganic geochemical characteristics of the concretions and surrounding rocks were analyzed using a series of techniques, including SEM, LA-ICP-MS, GC-MS-MS, and GC-IRMS. The concretions are composed of high content microcrystalline dolomite. The $\delta^{13}C_{carb}$ and $\delta^{18}O_{carb}$ values of the concretionary dolomite were significantly higher than those of the surrounding rocks. The dolomite show enrichment in the LREEs and have a negative Eu anomaly. The concretion biomarkers showed distribution characteristics similar to those of surrounding rocks. This suggested that the molecular fossils preserved in concretions were mainly inherited from surrounding rocks. However, the concretions contained more C_{27} sterane and hopanes, with the hopane/sterane ratio being significantly higher than that of surrounding rocks (1.49 v. 0.86). Moreover, the relative content of 2-methylhopane was 2.4–6.6 times that of the surrounding rocks. This indicated changes in the biological equilibrium of source organisms within and outside the concretions. It was possible that the unstable organic matter at the core increased the bacterial concentration and activity inside the concretions. Both the hydrogen index and biomarker-derived indicators implied that the transformation of organic matter in concretions was minimized when compared with their host rock. The isotope $\delta13C_{16\text{-}30}$ was 1‰–3‰ more prevalent in individual N-alkane hydrocarbons in the concretions than in surrounding rocks, likely owing to differences in lithology, bacterial action, and degree of weathering. The study concluded that carbonate concretions could preserve molecular fossils better than the surrounding rocks, and the in-depth organic geochemical analysis of concretions could provide a valuable reference for research into early life forms.

KEYWORDS

shale, carbonate concretion, molecular fossil, songliao basin, cretaceous

1 Introduction

Carbonate concretions of similar shapes but different sizes have been found in shales of many sedimentary basins around the world (Yemane and Kelts, 1996; Abdel-Wahab and Mcbride, 2001; Rabassa, 2006; Wanas, 2008; Lash, 2015; Plet et al., 2016; Dong et al., 2017; Lin et al., 2021) (Figure 1). For example, the long axis of carbonate concretions in Hanover shales in New York is about 10 cm. Lash (2015) found authigenic barite co-occurring with these calcium carbonate concretions (Figure 1A) and proved that the carbonate precipitated first. Lin et al. (2021) described carbonate concretions in the Cretaceous shale that were intermittently present along beddings (Figure 1B). Wu et al. (2021) proposed a conceptual ion transport model to interpret the growth mechanisms of calcareous concretions that were only a few centimeters in size in the varved sediments of a glacial lake (Figure 1C). Plet et al. (2016) studied pyritiferous calcite concretions in the Toarcian Posidonia Shale of southwestern Germany. Their study indicated that sulfate-reducing bacteria played a major role in concretion growth (Figure 1D). Carbonate concretions were also found in the outcrops of the marine-continental transitional facies strata (Figure 1E). The limestone and dolomite concretions in the Triassic Yanchang Formation in the southern Ordos Basin were studied by Dong et al. (2017). These concretions are believed to be products of early diagenesis, and their formation is related to the methane generated due to alkane production and microbial metabolic activity (Figure 1F). Large concretions, several meters in diameter, have been found in the Cambrian shales in southern China. They are well preserved, although the surrounding shale has been denuded (Figures 1G,H).

These concretions form inherent systems and preserve abundant geological information. Hence, they have varied significance and have become puzzles of immense research interest for geologists (Clifton, 1957; Woo and Khim, 2006; Lengger et al., 2017; Wu et al., 2021; Mojarro et al., 2022).

There are mainly three viewpoints surrounding the origin of carbonate concretions in shales. That is, there are three geochemical models. ① According to the equilibrium model, concretions grow in sediments where pore water is oversaturated with carbonates, and the sediments contain all kinds of (organic or inorganic) latent nuclei (from microscopic to macroscopic scale). Carbonates may begin to precipitate and grow around some favorable nuclei (Scotchman et al., 2000). ② The local equilibrium model suggests that at a shallow burial site, when microbial action (e.g., sulfate reduction) against an organic matter that acts as a nucleus is sufficiently fast, a specific microenvironment is created and maintained. Here, the concentrations of carbonates and other products are higher than in surrounding sediments, leading to carbonate oversaturation (Coleman, 1993; Khokhlova et al., 2021). ③ According to the mixed fluid model, in some areas, atmospheric precipitate or deep fluids get mixed with pore water, inducing the formation or maintaining the growth of carbonate concretions (Abedini and Calagri, 2017). Other theories suggest that the CO_2 produced due to the leakage of submarine natural gas hydrates combines with Ca^{2+} in seawater to form $CaCO_3$ (Ou et al., 2013), and underflow at the sediment–water interface promotes the interruption of argillaceous sedimentation, leading to the formation of concretions with early diagenesis (Jin, 1989). Of these hypotheses regarding the origin of carbonate concretions, the local equilibrium model—which considers that the biochemical action of microorganisms induces concretion formation—is supported by most studies (Coleman, 1993; Melendez et al., 2013; Lengger et al., 2017; Sun et al., 2021).

Carbonate concretions were generated during the synsedimentary to the early diagenetic stage. Hence, they are referred to as "time capsules" (Dale et al., 2014). Researchers believe that carbonate concretions have the potential to provide valuable information about the ancient Earth (Clifton, 1957; Melendez et al., 2013; Dale et al., 2014; Mavotchy et al., 2016). During and after the formation of carbonate concretions, an enclosed microsystem that is independent of and distinct from surrounding rocks is generated (Raiswell and Fisher, 2000; Railsback, 2021). Paleoenvironmental and paleontological information on the synsedimentary to the early diagenetic stage is sealed within this protected microsystem. In shale outcrops, carbonate concretions are commonly found to be intact ellipsoids and exhibit strong weathering resistance. The dolomitic concretions in shale outcrops in the Franceville Basin of Africa are considered one of the best-preserved sediments of the Proterozoic period (Mavotchy et al., 2016). In many calcium carbonate concretions, intact three-dimensional (3-day) fossils, undeformed sedimentary textures, and card-house-like clay structures have been found. This proves the capacity of carbonate concretions to resist compaction (Lash and Blood, 2004; Das and Tripathi, 2009). Authigenic carbonates in concretionary bodies can form an armor that blocks all types of external fluids during encapsulation, minimizing the chemical reactions of materials within the concretions (Raiswell and Fisher, 2000). The uranium levels in carbonate concretions in Cambrian Alum shales in Northern Europe are hundreds of times higher than those in surrounding shales (Yang et al., 2020). Evidently, carbonate concretions could serve as a "black box" for the ancient Earth.

Inorganic geochemical information is gradually extracted from carbonate concretions. Characteristics, including the isotopic compositions of the carbonates in concretions, can be applied in several ways. These include a reproduction of the paleo-elevation of the Qinghai-Tibet Plateau (Rowley and Currie, 2006), determination of the first period of oxygen elevation in the atmosphere (Mavotchy et al., 2016), estimation of the proto-ocean temperature (Mavotchy et al., 2016), analysis of basin fluids and diagenetic history (Hudson et al., 2001; Dale et al., 2014), and determination of the pH of ancient water and its redox state (Plet et al., 2016; Luo, 2020).

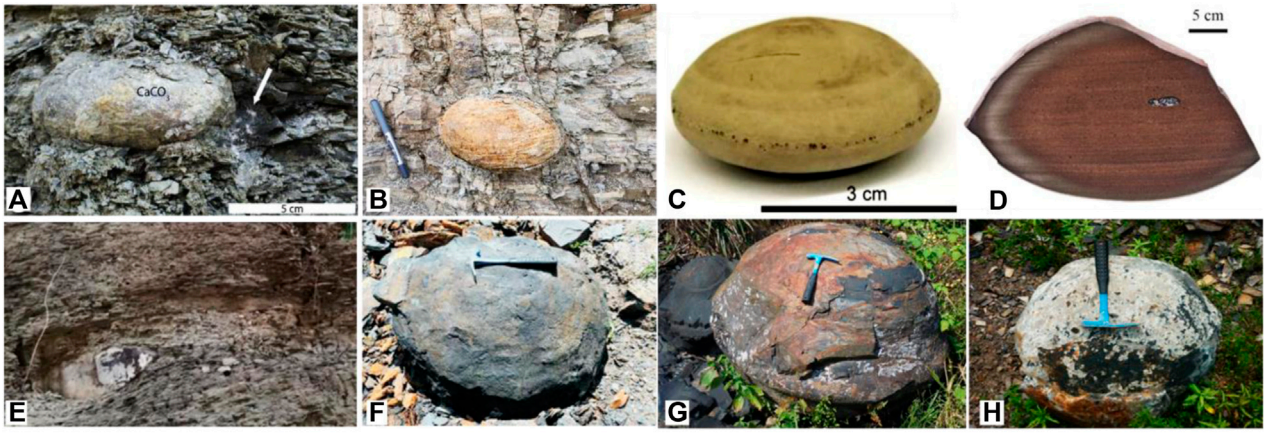

FIGURE 1
Carbonate concretions in shales. **(A)** Carbonate concretions in Hanover shales in New York, the United States. Carbonate concretion with barite (white arrow) filling a pressure shadow (Lash, 2015); **(B)** Carbonate concretions in Cretaceous Nenjiang shales in the Songliao Basin, China; **(C)** Carbonate concretions in Pleistocene mudstones in Connecticut, the United States (Wu et al., 2021); **(D)** Carbonate concretions in the Toarcian Posidonia shales in southwestern Germany (Plet et al., 2016); **(E)** Carbonate concretions in Shanxi-Taiyuan shales in Jiaozuo City, China; **(F)** Carbonate concretions in Yanchang shales in the Ordos Basin, China (Dong et al., 2017); **(G,H)** Carbonate concretions in Cambrian Niutitang shales in Chongqing, China.

In comparison, the applications of organic geochemical information derived from carbonate concretions are limited. The oldest fossil of a prokaryotic microorganism on Earth is preserved in the concretions of the Varauna group in the Archaeozoic Pilbara supergroup in Western Australia (Schopf, 1993, 2002). In recent years, some researchers have detected specific and semi-specific biomarkers, including methylhopanes, in concretions and discussed the biochemical action of sulfate-reducing bacteria and methanogens in the diagenetic stage (Plet et al., 2016). However, there has been little research on the differences in molecular fossil composition in different parts of concretions.

This study explored the biomarker composition of carbonate concretions in Cretaceous Nenjiang shales in the Songliao Basin (northeastern China) and compared them with surrounding shales. The organic geochemical differences between concretions and surrounding rocks were evaluated, and the preservation capacity of the concretions was assessed. The specific research objectives included: i) identifying signatures of molecular fossils and microbial activities; ii) using organic geochemical indicators to study the preservation characteristics of the carbonate concretions; iii) determining the significance of organic geochemical factors in such concretions.

2 Geology

The Songliao Basin is a Meso-Cenozoic lacustrine basin in northeastern China (Figure 2). The lacustrine shale of the upper Cretaceous Nenjiang formation is one of the most important hydrocarbon sources in the Songliao Basin (Wang et al., 2015; Liu et al., 2021). It was formed during the second expansion period of the Songliao Basin (Sun et al., 2006; Zhang et al., 2022). The first and second members at the bottom of the Nenjiang formation are organic-rich shales of semi-deep and deep lacustrine facies (Figure 2). The organic matter in the first member is mainly of type II_1, with a total organic carbon content (TOC) of 0.1%–9.90% (2.65% on average). In the second member, the organic matter is dominated by type II_1 and II_2, with a small amount of type III, and TOCs of 0.47%–11.19% (1.80% on average). Moreover, a gradual transition to gray argillaceous siltstone and siltstone is observed as we move from the third to the fifth member of the formation (Liu et al., 2020).

3 Samples

Samples were collected from the south of the Songliao Basin near the Yaojia Railway Station (Dehui County, Jilin Province, China) (Figure 3A). The first and second members of the Nenjiang formation are outcropped, and the vertical thickness reaches 30 m. Rocks in this area mainly include dark-gray and gray shales interbedded with thin layers of gray silty mudstones and limestone (Figure 3B) with an isotopic age of 81.8 Ma (Lin et al., 2021). The carbonate concretions are present intermittently along the beddings and show clear boundaries with surrounding rocks. They are commonly oblate ellipsoids with a flat horizontal surface parallel to the beddings (Figure 3C).

At the outcrop, there are shale beddings surrounding the concretions, indicating that the carbonate concretions were

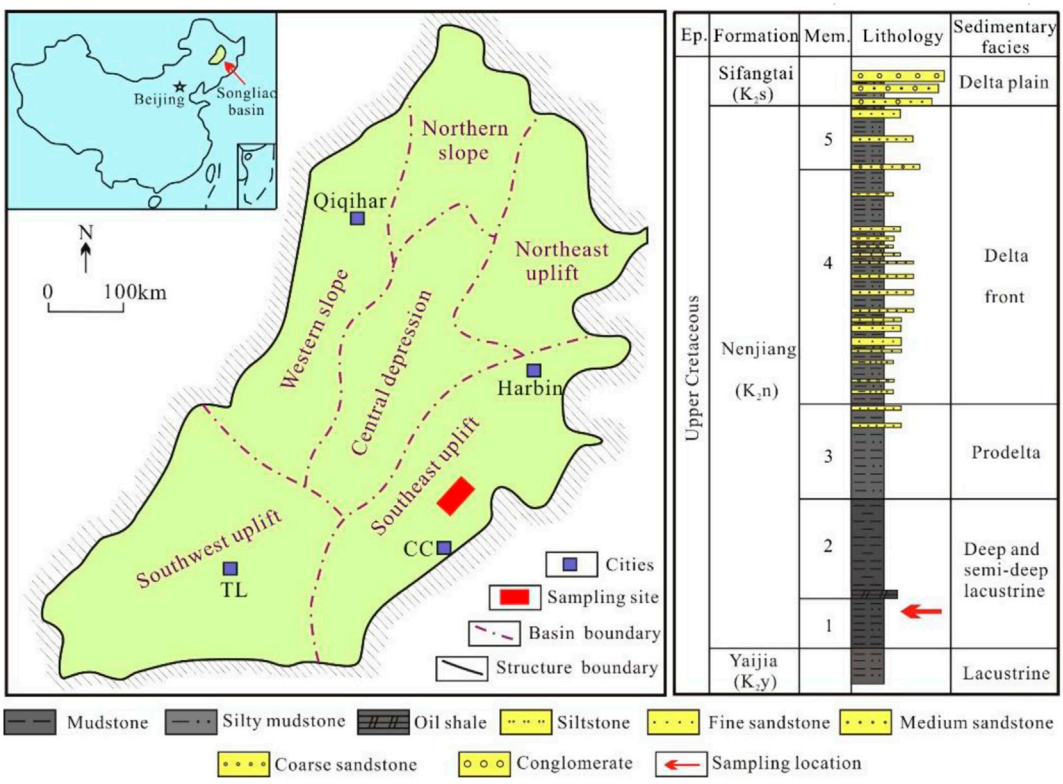

FIGURE 2
Location of the sampling site in the Songliao Basin and stratigraphic profile of the Nenjiang Formation.

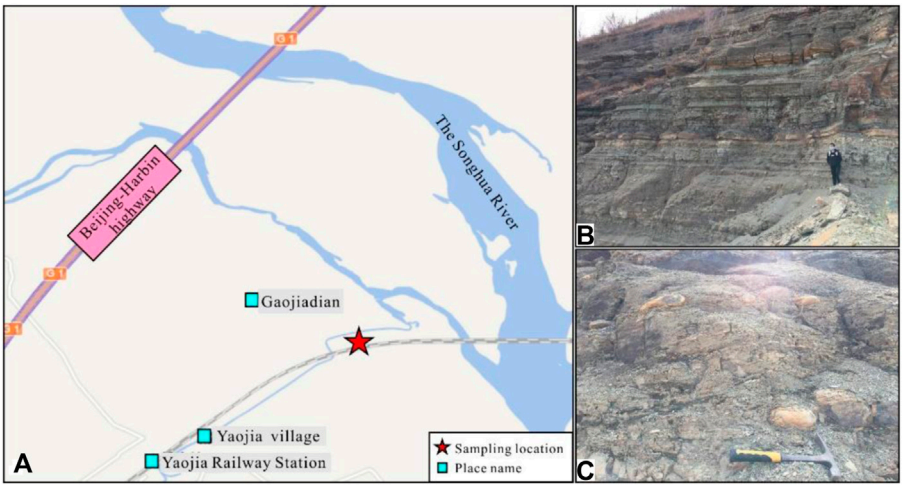

FIGURE 3
Location of the sampling site and field photographs. **(A)** Location of the sampling site, southeast of the Songliao Basin; **(B)** Sampling profile; **(C)** Concretion outcrop.

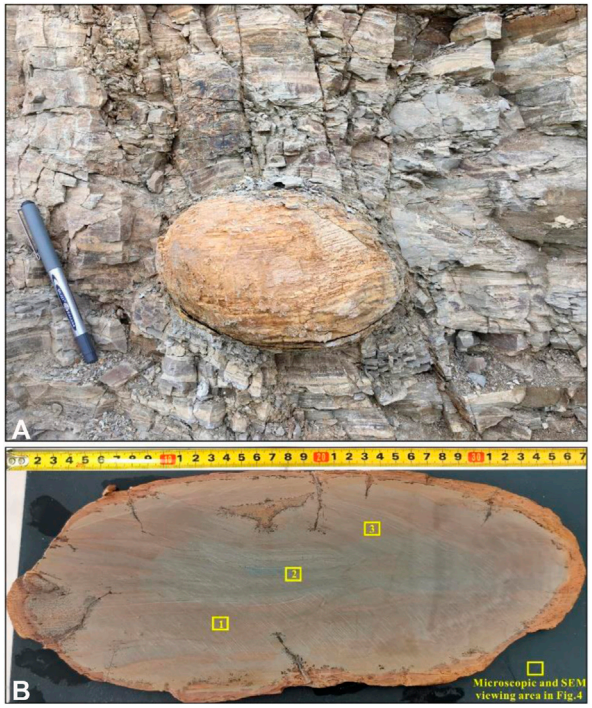

FIGURE 4
Images of concretions. **(A)** Field occurrence of the concretion; shale beddings surrounding the concretions were present; **(B)** Longitudinal profile of the concretion. No obvious lamellae were observed in the main body of the concretions, except at the core. The concretion had a clear shell.

formed at the synsedimentary stage (Figure 4A). Two concretions embedded in shales (both ellipsoids) were collected along with their surrounding rocks. The long axis, short axis, and weight of the first concretion were 273 mm, 223 mm, and 8.65 kg, while those of the other were 255 mm, 174 mm, and 7.95 kg, respectively. The weights of all samples met the requirements for subsequent testing.

The concretions were cut across their centers, and their internal structures were observed in this plane (Figure 4B). The concretionary bodies were dark-gray carbonatites. Except for the core, which had a lamella-like structure, no obvious beddings were observed in the main body of the concretions. A clear shell composed of khaki carbonatites that readily spalled from the surface could be observed. V-shaped fractures were induced around the concretions and ran through the shell, propagating inwards over a length no longer than 60 mm. Most fractures were filled (Figure 4B).

4 Methods

Organic contaminants were removed from the surface of the samples. Most tests were conducted by separately sampling from different locations, including the core, main body, shell, and rock surrounding the concretions, facilitating systematic comparison.

① X-ray diffraction (XRD): Whole-rock-powder XRD was adopted to identify mineral species at five locations in the samples. All concretion and surrounding rock samples were examined using a D/max-2,500PC diffractometer (Rigaku, Japan). Data were obtained within the range $5^{\circ}C \leq 2\theta \leq 60^{\circ}C$ (in increments of $0.015^{\circ}C$ and 0.7 s).
② Scanning electron microscopy (SEM): A COXEM EM-30 scanning electron microscope and a Zeiss microscope were used to observe the microstructures of concretion slices.
③ Laser ablation inductively coupled plasma mass spectrometry (LA-ICP-MS): Major and trace elements at 13 measurement points across different locations in the concretions were analyzed using LA-ICP-MS. These measurement points were located on the shell (point 1), edge (points 2 and 3), main body (points 4–8), and core (points 9 to 13 on different lamellae).
④ Stable isotopes of carbonates: An IsoPrime100 isotope ratio mass spectrometer (Elementar, Germany) was employed to detect the stable C and O isotopic composition of the carbonates in the six samples. The Pee Dee Belemnite standard was applied for the isotopes, and the standard deviation in all repeat analyses was less than 0.1‰.
⑤ Whole-rock organic geochemistry: HCl was used to remove inorganic carbons, and subsequently, standard organic geochemical analysis was performed on aliquots of dried residues. A CS844 analyzer was used to estimate the TOC of the samples. The hydrogen index (HI) was detected using a YQ-VIIIA oil-gas display and evaluation instrument
⑥ Gas chromatography-mass spectrometry (GC-MS): The Soxhlet extraction method was used for the extraction and separation of group-specific components in powdered samples of the concretionary bodies, shells, and surrounding rocks. GC-MS analysis for the aliphatic series and aromatic components was conducted on an Agilent 7890A GC/5975C MSD chromatograph-mass spectrometer equipped with a DB5-MS chromatographic column measuring 0.25 mm × 60 m × 0.25 μm. The initial temperature was $60^{\circ}C$. It then increased to $300^{\circ}C$ at a rate of $4^{\circ}C$/min; at this constant temperature, the retention time was 40 min. Ultra-high-purity helium was used as the carrier gas. The gas flow was maintained at 1 ml/min. The temperature of the ion sources was $250^{\circ}C$.
⑦ Gas chromatography-tandem mass spectrometry (GC-MS-MS): To improve test accuracy and identify the presence and types of methylhopanes, an Agilent 7010B Chromtech Evolution gas chromatography-tandem mass spectrometer was used to study alkane components of the concretion sample A in the multiple reaction monitoring (MRM) modes. A 60-m DB5-MS chromatographic column was used, with the film thickness and inner diameter being 0.25 μm and 0.25 mm, respectively. Helium was used as the carrier gas. The gas flow rate was 1.5 ml/min. The test temperature was programmed to increase at a rate of $4.0^{\circ}C$/

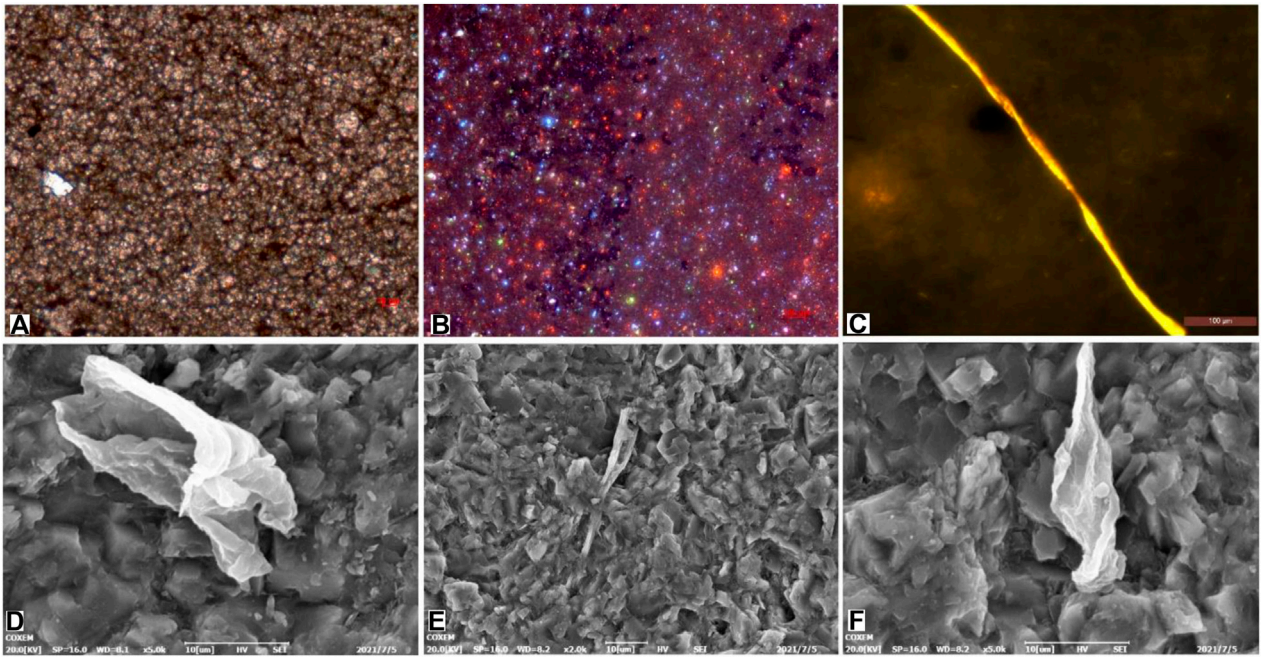

FIGURE 5
Optical, cathodoluminescence, and scanning electron microscopy (SEM) images of the concretions. (The test areas are shown in Figure 4B. Images A and B are derived from box 1 in Figure 4B. Image C is derived from box 2 in Figure 4B. Images D, E, and F are derived from box 3 in Figure 4B.). **(A)** Transmission light microscopy shows that the microcrystalline dolomite in the concretions occurs homogeneously. **(B)** Cathodoluminescence microscopy revealed that dolomite shows orange-red fluorescence. **(C)** Fluorescence microscopy revealed organic matter. **(D–F)** SEM showed microfossils.

min from 60°C to 300°C. Ion sources were maintained at 250°C and 70 eV. The temperature of the vaporizing chamber was 300°C. Methylhopanes were identified by monitoring the ion fragments at 412 to 205, 426 to 205, 440 to 205, 454 to 205, 468 to 205, 482 to 205, and 96–205 Da.

⑧ Gas chromatography-isotope ratio mass spectrometry (GC-IRMS): Saturated hydrocarbons were purified to obtain the N-alkane components. Then, a continuous flow stable isotope ratio mass spectrometer (GC/EA/GC-Isoprime 100) was used to detect the carbon isotopes in individual pure N-alkanes. The gas chromatographic column, carrier gas, feeding conditions, and temperature programming were similar to those used for GC-MS analysis. The value of $\delta^{13}C$ was expressed as per mileage (‰) based on the Pee Dee Belemnite (PDB) standard. Each sample was tested twice to determine the measurement accuracy.

5 Results

5.1 Composition and microstructure

According to the XRD test, the concretionary bodies contained more than 90% (weight) of dolomite, 3%–4% of quartz and feldspar, 2%–3% of clay minerals, and small amounts of apatite and aragonite. The shell contained 77% dolomite, 10% quartz and feldspar, and 10% clay mineral, which was more than that in the concretionary bodies. The contents of carbonates, clay minerals, quartz, and feldspar in the surrounding rocks were 10%, 15%–20%, 45%, and 20%–25%, respectively.

The main body and core of the concretion were observed under a light microscope and scanning electron microscope. The test areas are shown in Figure 4. The shell and surrounding rock were too fragile and could not be used for sample preparation. Under the optical microscope, microcrystalline dolomite was found to be homogeneously present in the concretions (Figures 5A,B). Minute crystals of dolomite showing orange-red fluorescence were observed under a luminescence microscope (Figure 5B). This indicated that they precipitated rapidly and were primary minerals. On the microscopic scale, there was no bedding structure. SEM showed microfossils of algae and acritarchs sized 10 μm–20 μm dispersed in the concretions. These were mainly shaped like slender rods or curls. Notably, 3-day structures could be clearly observed (Figures 5C–F).

5.2 Stable carbonate isotopes

The examination of stable carbonate isotopes at different locations indicated that the concretions contained high values of

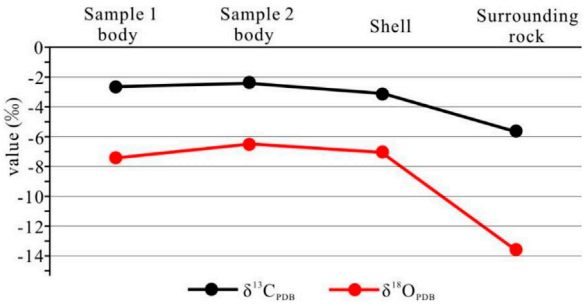

FIGURE 6
Comparison of $\delta^{13}C_{carb}$ and $\delta^{18}O_{carb}$ values of carbonates at different locations.

FIGURE 7
Locations of measurement points for the elemental analysis of concretion A.

$\delta^{13}C_{carb}$ and $\delta^{18}O_{carb}$, ranging from −2.4‰ to −2.6‰ and −6.5‰ to −7.4‰. The isotope profiles of concretion shells were comparable to those of the main body of the concretion. In comparison, the $\delta^{13}C_{carb}$ and $\delta^{18}O_{carb}$ values were significantly lower in surrounding rocks (−5.6‰ and −13.6‰) (Figure 6).

5.3 Elemental compositions

The major and trace element compositions were examined at 13 measurement points (Figure 7) from the center to the edge across the transverse profile of concretion A using LA-ICP-MS. The values are listed in Table 1.

LA-ICP-MS, Laser ablation inductively coupled plasma mass spectrometry; REE, rare Earth elements; LREE, light rare Earth elements; HREE, heavy rare Earth elements.

According to the test results, Ca and Mg were the most abundant elements in the concretions, followed by Si, Na, and Al. The S and Fe contents were relatively low but tended to increase gradually toward the edge (Table 1). The concretions were characterized by a high abundance of Sr and Mn (Sr abundance: 930.1 ppm–2,706.8 ppm; Mn abundance: 477.7 ppm–1976.1 ppm) and a low abundance of Fe (184.6 ppm–644.9 ppm).

The total rare Earth element (REE) content (∑REE) in the concretionary body ranged from 26.35 μg/g to 256.94 μg/g, averaging at 106.92 μg/g. The total contents of light REEs (LREEs) and heavy REEs (HREEs) were 5.40 μg/g–217.98 μg/g and 3.73 μg/g–38.96 μg/g, respectively, and the LREE/HREE differentiation coefficient ranged from 1.66 to 11.93. This suggested that the concretions were relatively enriched for LREEs (Figure 8A). The Ce and Eu anomaly values of samples were calculated using the $Ce/Ce^* = Ce_N/(La_N + Pr_N)^{0.5}$ and $Eu/Eu^* = Eu_N/(Sm_N \times Gd_N)^{0.5}$ formulae (Taylor and McLennan, 1985). In these equations, N refers to the normalization value of REEs. The Eu/Eu* value showed a negative anomaly and was in the range of 0.46–0.96 (0.77 on average). The Ce/Ce* value ranged from 0.77 to 1.36, indicative of a moderate positive or negative anomaly (Figure 8B). Contrasting characteristics were observed at points 11 to 13 in the core, where the ∑REE values were far higher than those in the concretionary body (803.04 μg/g–1,009.78 μg/g) (Figure 8A). In addition, the LREE/HREE ratio was smaller than 1 (0.74–0.82) (Figure 8A), indicating the slight enrichment of HREEs. The Eu/Eu* value showed a positive anomaly, while the Ce/Ce* value exhibited a negative anomaly. (Figure 8B).

REE, rare Earth elements; LREE, light rare Earth elements; HREE, heavy rare Earth elements.

5.4 Composition and preservation of molecular fossils

5.4.1 Organic carbon and HI

The TOCs of concretions A and B were similar to those of surrounding rocks (~0.8%), although the values were slightly lower in the concretions. In contrast, the HI was significantly higher in the concretions. The HI at four measurement points in the concretions ranged from 86 mg/g to 122 mg/g TOC, being 106 mg/g TOC on average. In the surrounding rocks, the HI at four measurement points was 41 mg/g–50 mg/g TOC, with an average of 46 mg/g TOC.

Through pyrolysis, it was found that the T_{max} of the concretion samples was 430°C–437°C and that of surrounding rocks was 432°C–447°C. GS-MS analysis results indicated that the 22S/(22S+22R) ratio of C_{31} hopane and the 22S/(22S+22R) ratio of C_{32} hopane were both lower than 0.5, suggesting that the organic matter was not highly mature.

5.4.2 Biomarkers and biomarker-derived indicators

Samples of the concretionary bodies, shells, and surrounding rocks showed similar biomarker compositions (Figure 9). The main peak of lipid biomarkers was observed for medium-chain alkanes (C_{22}-C_{25}), which indicates that the organic matter was dominated by aquatic plants. The

TABLE 1 Elemental composition determined using the LA-ICP-MS analysis.

Point no.	1	2	3	4	5	6	7	8	9	10	11	12	13
Na (wt%)	0.30	3.97	12.63	1.20	1.35	3.82	3.05	0.97	0.42	1.39	2.70	9.37	3.81
Mg (wt%)	1.52	9.95	8.60	12.14	14.05	15.36	11.18	10.82	5.67	4.94	11.52	8.24	9.40
Al (wt%)	0.89	2.17	3.93	1.59	1.73	2.13	2.02	2.15	0.82	2.97	2.51	3.30	1.85
Si (wt%)	7.15	11.46	14.86	7.28	5.77	7.44	6.56	6.81	4.55	12.49	8.11	12.39	9.17
S (wt%)	0.036	0.031	0.030	0.028	0.028	0.028	0.028	0.027	0.027	0.026	0.026	0.026	0.026
K (wt%)	0.09	0.05	0.08	0.06	0.05	0.10	0.12	0.10	0.04	0.10	0.08	0.05	0.04
Ca (wt%)	15.35	16.63	9.37	18.44	21.42	18.99	10.68	15.32	14.57	8.77	14.55	7.13	13.80
Mn (ppm)	1950.12	1,224.59	932.86	1,328.43	1,192.79	825.09	541.69	615.66	477.74	1,338.88	606.97	1,482.75	1976.11
Fe (ppm)	644.86	398.45	489.31	574.30	373.56	287.09	184.58	286.81	186.67	266.72	229.59	278.08	262.92
Cu (ppm)	18.25	4.70	10.33	6.56	4.01	10.48	7.83	12.07	4.38	6.85	11.22	8.84	4.15
Sr (ppm)	2077.30	2,299.49	1,557.78	2,382.92	2,706.77	2,176.04	1,506.54	2042.13	1987.82	1,345.15	2093.09	930.08	1752.16
Pb (ppm)	6.98	4.96	5.21	9.77	2.10	11.45	11.95	12.70	9.64	6.44	6.66	4.90	3.25
U (ppm)	4.80	2.51	4.50	3.73	6.46	2.72	1.26	3.14	2.24	2.60	3.10	0.98	1.53
Th (ppm)	5.62	2.49	4.85	3.53	7.14	2.98	1.34	3.16	2.58	2.75	3.78	1.03	1.48
La (ppm)	0.04	47.28	11.60	14.78	28.71	47.00	4.06	10.16	10.81	13.67	57.32	72.66	53.74
Ce (ppm)	0.30	99.87	24.70	23.84	52.91	98.52	7.72	20.53	22.15	29.56	64.47	84.44	59.62
Pr (ppm)	0.00	12.48	3.59	2.53	6.30	9.35	0.77	2.35	2.23	3.04	62.05	78.71	60.42
Nd (ppm)	0.02	45.89	14.65	9.76	21.32	32.15	2.89	8.32	7.51	11.11	57.49	71.19	53.78
Sm (ppm)	0.01	10.31	3.09	2.03	4.15	6.35	0.79	1.70	1.40	2.27	61.52	76.05	58.27
Eu (ppm)	0.00	2.16	0.83	0.70	1.09	1.34	0.20	0.38	0.39	0.60	58.04	70.33	56.18
Gd (ppm)	0.00	10.17	3.73	2.29	4.31	5.71	2.32	1.35	1.32	2.03	59.16	72.06	59.11
Tb (ppm)	0.00	1.56	0.56	0.30	0.63	0.75	0.51	0.19	0.12	0.29	59.44	70.44	56.97
Dy (ppm)	0.01	10.35	3.86	1.69	3.71	4.53	3.03	1.25	0.90	1.55	55.52	65.79	54.36
Ho (ppm)	0.01	2.02	0.86	0.39	0.72	0.91	0.56	0.29	0.18	0.30	59.76	70.23	57.97
Er (ppm)	0.00	6.18	2.36	1.20	1.96	2.75	1.59	1.12	0.48	0.98	60.68	69.41	59.44
Tm (ppm)	0.00	0.86	0.40	0.22	0.30	0.40	0.24	0.14	0.09	0.12	57.03	66.86	56.35
Yb (ppm)	0.01	6.83	3.32	1.59	2.03	3.06	1.51	1.40	0.58	1.14	62.20	73.64	60.53
Lu (ppm)	0.00	0.99	0.51	0.23	0.34	0.52	0.19	0.23	0.08	0.17	58.57	67.96	56.31
ΣREE	0.41	256.94	74.04	61.54	128.48	213.32	26.35	49.40	48.22	66.82	833.25	1,009.78	803.04
LREE/HREE	11.03	5.60	3.75	6.78	8.18	10.45	1.66	7.30	11.93	9.17	0.76	0.82	0.74
Ce/Ce*	5.76	0.96	0.90	0.91	0.92	1.10	1.02	0.98	1.06	1.07	0.25	0.26	0.24
Eu/Eu*	0.00	0.65	0.76	1.00	0.80	0.69	0.46	0.78	0.89	0.86	2.97	2.93	2.96

abundance of steranes pointed to the huge contribution of algae. Meanwhile, alkanes with a molecular weight as high as C_{37} exhibited a low abundance. In surrounding rock samples, the content of long-chain alkanes (C_{30}-C_{33}) was significantly higher (Figure 9), indicating the contribution of higher terrestrial plants. In the shell, the lipid biomarkers demonstrated the transition characteristics between the body of the concretions and the surrounding rocks.

The high gammacerane ratio (2.6–3.3) of the samples suggested the presence of water stratification at the sedimentary stage. The pristane/phytane (Pr/Ph) ratio was low throughout (0.39–0.48), indicating that the concretions were formed in a strongly reducing saltwater environment. Except for C_{27}, a series of complete 13β14αC_{19}-C_{29} tricyclic terpenes also appeared on the m/z = 191 chromatograms (Figure 9).

ααα20R C_{29}, C_{27}, and C_{28} were the primary steroids present in the samples, which had a low abundance of αββ isomers. The samples also contained a small amount of C_{30}, C_{21}, and C_{22} steranes. In each group of samples, the proportion of C_{29} sterane was the highest. The concretionary body samples contained higher amounts of C_{27} sterane and C_{27} rearranged sterane. The C_{27} sterane content and the C_{27}/C_{29} ratio were highest in concretionary bodies, followed by shells and surrounding rocks. The ratio of rearranged to regular steranes was relatively low (0.01–0.12), indicative of low maturity.

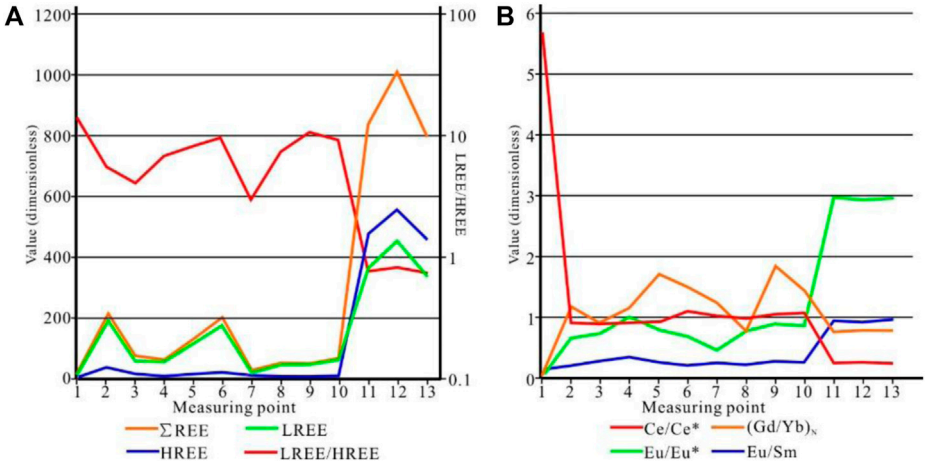

FIGURE 8
REE contents at various measuring points **(A)** and characteristic parameters **(B)**.

The detected hopanes were between C_{27} and $C_{35,}$ and the distribution of (17α, 21β and 17β, 21α) $C_{31\text{-}35}$ homohopanes was similar across samples from different groups (Figure 10). Except for C_{33} homohopane in concretionary body samples, which had a slightly lower abundance than that in host shale samples, C_{31} to C_{35} homohopanes all showed a higher abundance in the concretionary body than in surrounding rocks. Hopane-derived maturity indicators, including the Ts/(Tm+Ts) ratio, $C_{29}T/(C_{29}$ hopane + $C_{29}T)$ ratio, and $C_{31\text{-}35}$ 22S/(22S + 22R) homohopane ratio, showed different values in samples of concretionary bodies and surrounding rocks. Surrounding rock samples had a high conversion degree of these organic compounds. The βα/(αβ + βα) $C_{29\text{-}31}$ indicator also revealed a lower organic matter maturity in the concretions.

The hopane/sterane ratio of concretionary bodies was significantly higher than that of the surrounding rocks (concretionary bodies *v.* shells *v.* surrounding rocks = 1.49 *vs.* 0.92 *vs.* 0.86), indicating certain differences in their ecological structures.

Crocetane, which is specific to anaerobic methane oxidation, was not detected in the concretions or surrounding rock samples. This may be because it is difficult to detect due to the interference of N-alkane ion fragments that show stronger responses (Xu et al., 2022). The abundance of 3β-methylhopane, which is semi-specific for methane-oxidizing bacteria, was relatively low (Wakeham et al., 2004). These results indicated that the contribution of these microorganisms to the growth of concretions was limited.

Methylhopanes, derived from 2- and 3-methylbacteriohopanepolyols produced by bacteria, were used to study the mediation effect of bacteria and the origin of organic matter. MRM analysis revealed the presence of C_{30} to C_{35} methylhopanes (Figure 11) in both the concretions and surrounding rock samples. 2α-methylhopane was the predominant methylhopane, while the abundance of 3β-methylhopane was low.

5.5 Carbon isotopes of individual hydrocarbons

In each group of samples, the $\delta^{13}C_{16\text{-}32}$ value of *n*-alkanes ranged from −33.6‰ to −28.4‰, with distributions being similar across groups (Figure 12). The carbon isotope ratio of medium-chain N-alkanes was 2‰–3‰ lighter than the short-chain and long-chain carbon isotopic compositions, indicating that the source microorganisms mainly lived under the water euphotic zone (Wang et al., 2015) and were rapidly buried and preserved after death. The $\delta^{13}C$ of long-chain *n*-alkanes behind nC_{28} changed greatly and was distributed in a zig-zag manner. The $\delta^{13}C_{29}$ and $\delta^{13}C_{31}$ of odd-number carbons were rich in ^{13}C while $\delta^{13}C_{30}$ was as low as −33.6‰.

Compared with concretionary bodies (average $\delta^{13}C$ of −29.9‰), surrounding rocks showed lighter $^{13}C_{16\text{-}32}$ contents, i.e., −32.0‰ on average. The average $\delta^{13}C$ of shell samples was −31.0‰, between that of concretionary bodies and surrounding rocks. The transitional feature of the shell suggests that the degree of biochemical interaction between the concretion and the surrounding rock is different, and the concretion is a relatively independent system.

6 Discussion

In order to determine the ability of carbonate concretions to preserve molecular fossils as an independent system, this paper

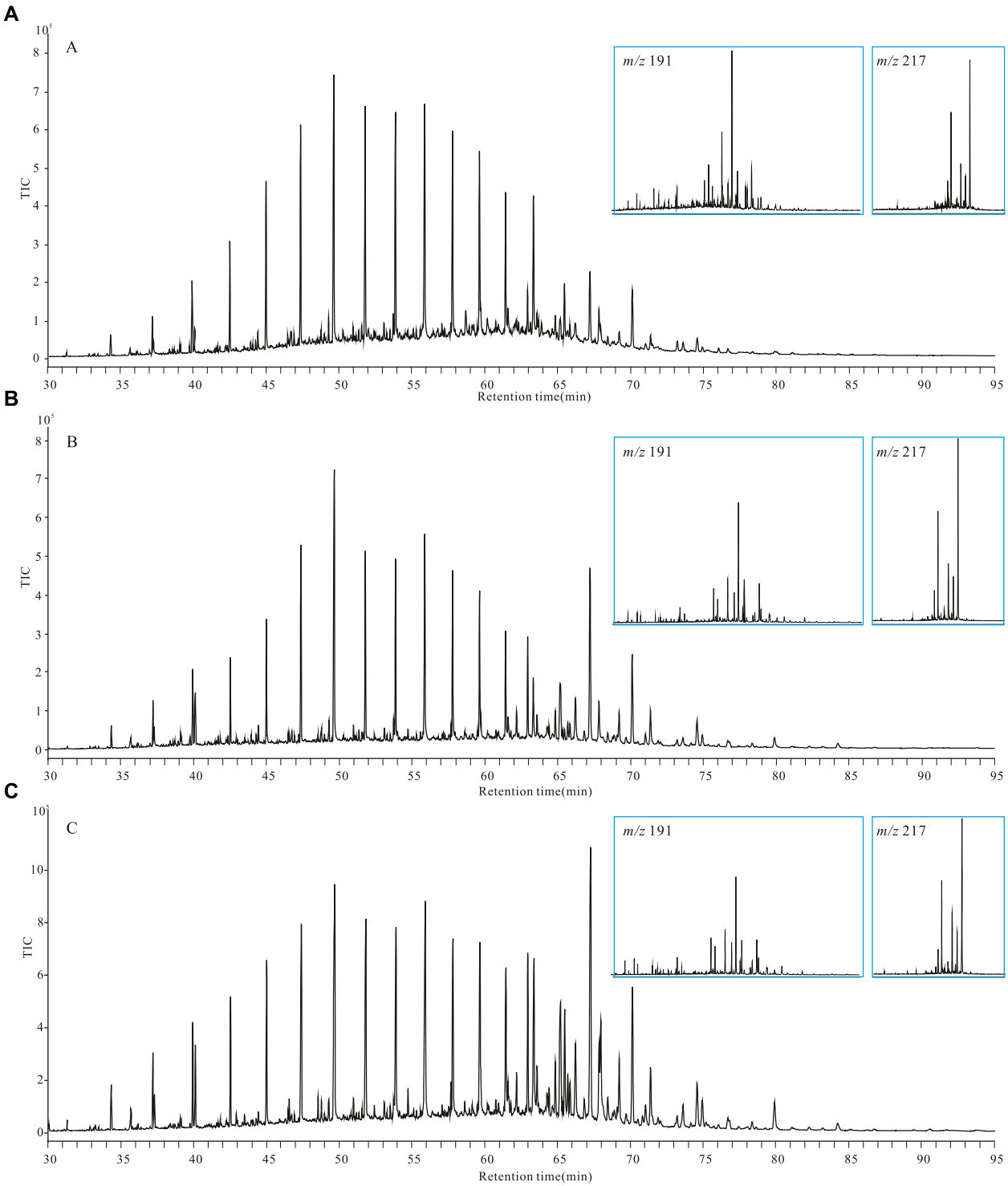

FIGURE 9
Gas chromatography-mass spectrometry chromatograms of the lipid fraction **(A)** Body of concretion A; **(B)** Shell of concretion A; **(C)** Host shale.

discusses the geochemical (inorganic and organic) characteristics of various parts of the concretion and the interior and exterior of the nodules according to the above test results. In this study, the high-content microcrystalline dolomite was found to occur homogeneously in the concretions. This was consistent with characteristics of rapidly precipitating phases of carbonates

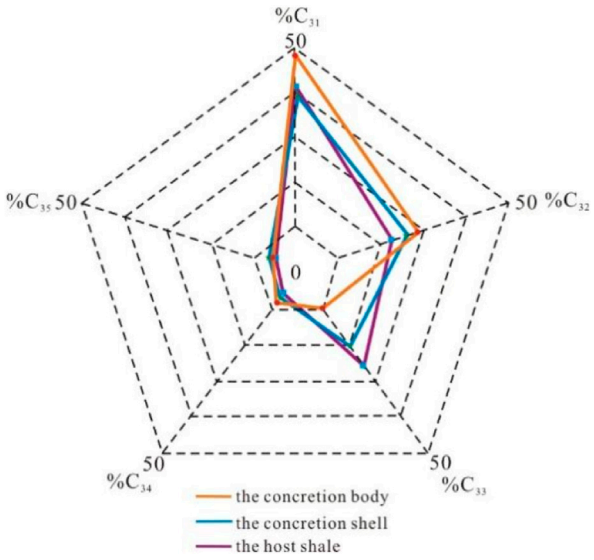

FIGURE 10
Homohopane content in the concretion body, shell, and host shales.

induced by microbial action. The high Sr and Mn contents in the concretions indicated the presence of hot and arid climatic features and were also related to the microbial mineralization of Mn and Sr ions (Tazaki and Morii, 2008).

Some REE parameters such as the LREE/HREE, Eu/Eu*, and Ce/Ce* ratios can be used to elucidate the formation mechanisms of sedimentary rocks such as limestone (Abedini and Calagri, 2017; Abedini et al., 2018, 2020; Abedini and Khosravi, 2022). According to the curves of the REEs parameters in all samples (Figure 8), the total REE content, Eu/Eu*, Ce/Ce*, and LREE/HREE value differed significantly among points 11–13 in the core, points 2–10 in the body, and point 1 in the shell of the concretions. This suggests that the concretion could be divided into three parts, each with distinct material sources or formation mechanisms.

Points 11–13 in the core of the concretions showed higher ∑REE and Eu/Eu* values than the points in the concretionary body. In addition, the LREE/HREE ratio and Ce/Ce* value at these points were lower than those in the concretionary body (Figure 8). These characteristics were similar to the geochemical characteristics of REEs found previously in organisms and biological fossils. The characteristics of REEs in biological fossils are mainly determined by the fractionation of REEs by the organisms and adsorption and metasomatism after sedimentation. Using an electronic probe and XRD, organic matter containing 78.4% carbon and apatite and aragonites related to biochemical action were found at points 11–13. Points 2–10 in the body of the concretions showed different characteristics. The loss of Eu suggested a weak-reducing and weak-oxidizing sedimentary environment. The Ce/Ce* value, also considered an effective tracer for redox environments, can indicate the depth of ancient lakes, as larger Ce/Ce* values point to deeper lake waters. Point 1 in the shell of the concretion showed the characteristics of weathered residues. In an oxidizing environment, Ce^{3+} is likely to be oxidized to Ce^{4+} (as CeO_2) and therefore get preserved in the elurium, leading to the strong enrichment of Ce. As a result, the Ce content can become seven-fold higher after weathering than that in the original rock.

The HI is a reliable indicator that aids in characterizing the source and degree of organic matter conversion. In this study, the HI was evidently higher in concretion bodies. Because the concretions and surrounding rocks share the same source of organic matter, the difference in HI is indicative of differences in organic matter conversion. The high HI indicates that the degree of organic matter degradation in concretions was definitely lower than that in the surrounding rocks.

In this study, the samples of concretionary bodies were found to contain higher contents of C_{27} sterane and C_{27} rearranged sterane. This characteristic is akin to that of concretions in the Gogo shale in the west of Australia (Lengger et al., 2017) and the Posidonia shale in the southwest of Germany (Plet et al., 2016). The proportion of C_{27} sterane gradually decreased while that of C_{29} sterane increased outwards from the interior of the concretions. Differences in the relative abundances of eukaryotic biomarkers suggest that the ecosystem equilibrium of the source organisms varied, or that the C_{27} sterane outside the concretions was degraded before the C_{29} sterane. C_{27} sterol is generally present at high levels in animals, and the extra C_{27} sterane in the concretions is likely associated with the unstable organic matter nuclei that initially triggered the formation of the concretions. In other words, the extra C_{27} sterane was likely derived from the sterol in the organic matter nuclei. As expected, the ratio of rearranged to regular steranes in surrounding rocks was higher than that in the concretions. This is because the conversion from steranes to rearranged steranes is catalyzed by clay minerals (Nabbefeld et al., 2010). Hence, the conversion rate is lower in carbonate concretions than in mudstones.

The differences and similarities in the composition of homohopanes between concretionary bodies and surrounding rocks imply that the bacterial communities that participated in the formation of the concretions were similar to those present in the surrounding sediments, and thus, no different homohopanes appeared. Because the concretions contain unstable organic matter with high local concentrations, the activities of the bacterial community present in the concretions were enhanced. The hopane-derived maturity indicators revealed the lower maturity of organic matter in concretions. The hopane/sterane ratio in concretionary bodies was greater than 1.0 (Table 2), indicating a greater abundance of prokaryotic bacterial and blue-green algal origins in the concretionary bodies. In comparison, the hopane/sterane ratio in surrounding rocks was less than 1.0, suggesting a slight predominance of eukaryotic origin.

2-methylhopane was previously considered a cyanobacterial biomarker. However, it is now known that many different

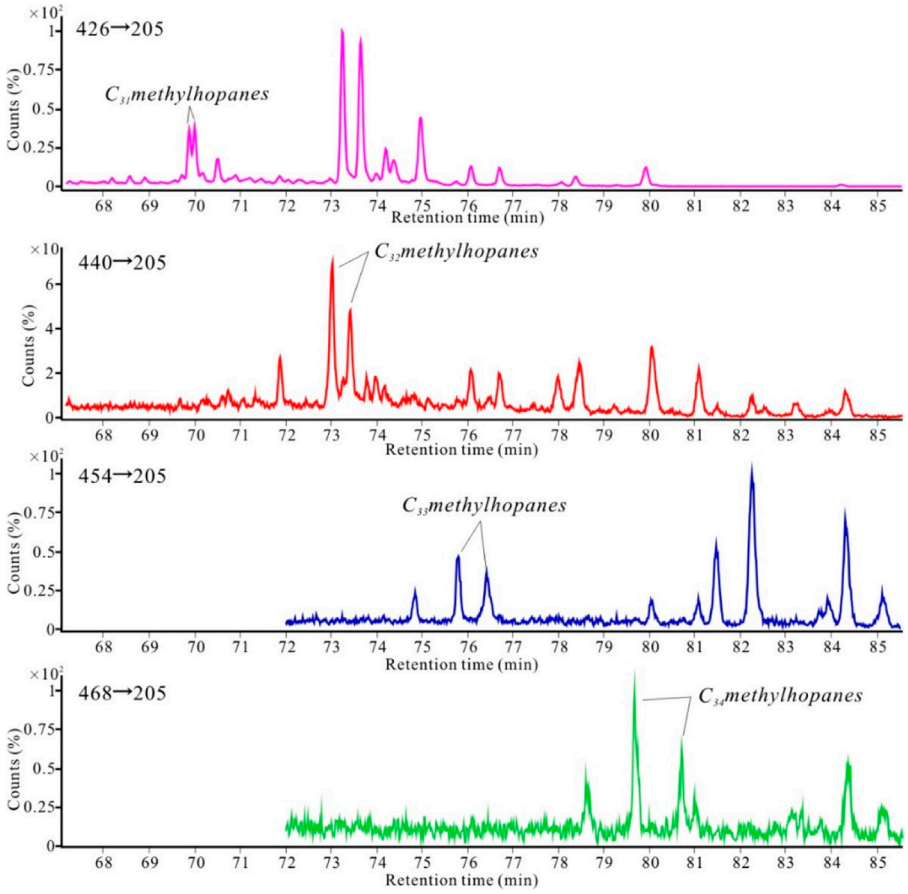

FIGURE 11
Gas chromatography-tandem mass spectrometry chromatograms of the methylhopane series in the body of concretion A.

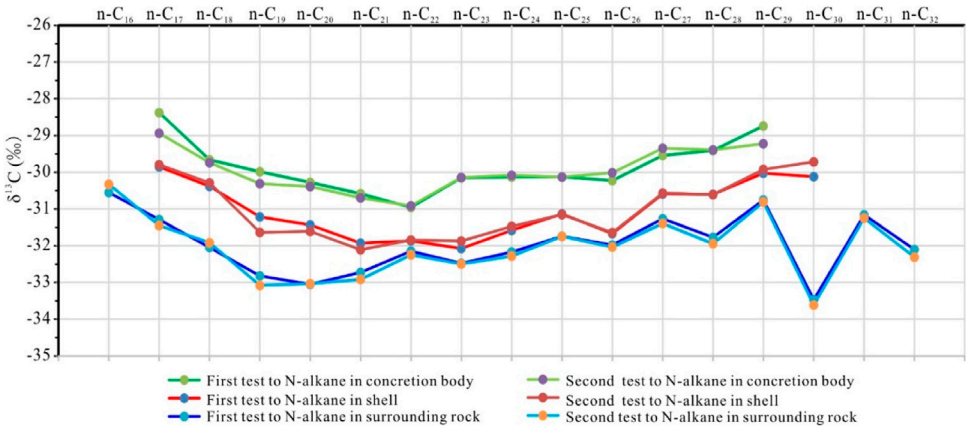

FIGURE 12
Gas chromatography-isotope ratio mass spectrometry results showing the $\delta^{13}C$ of *n*-alkanes.

TABLE 2 Biomarker ratios for the concretions and host shale.

Biomarker parameters	Concretions	Shell	Surrounding rocks
Pristane/phytane	0.48	0.39	0.41
% C_{27} steranes	26.19	22.20	20.48
% C_{28} steranes	17.63	19.82	22.16
% C_{29} steranes	56.18	57.97	57.36
C_{27} steranes/C_{29} steranes	0.47	0.38	0.36
C_{30} steranes/(C_{27-C30}) steranes	0.033	0.020	0.024
C_{27} diasteranes/(C_{27} + C_{28} + C_{29}) diasteranes	0.49	0.41	0.37
C_{28} diasteranes/(C_{27} + C_{28} + C_{29}) diasteranes	0.27	0.37	0.40
C_{29} diasteranes/(C_{27} + C_{28} + C_{29}) diasteranes	0.24	0.22	0.23
Diasteranes/steranes	0.009	0.015	0.121
% C_{31} homohopanes	48.36	40.48	41.68
% C_{32} homohopanes	29.04	26.66	22.78
% C_{33} homohopanes	9.95	20.74	25.93
% C_{34} homohopanes	7.61	6.22	5.13
% C_{35} homohopanes	5.05	5.90	4.48
C_{31} hopane/C_{30} hopane	0.19	0.25	0.33
C_{29} hopane/C_{30} hopane	0.32	0.43	0.44
10×Ga/(Ga + C30 hopane)	3.13	3.25	2.62
C_{35} homohopane 22S/(22S + 22R)	0.25	0.29	0.44
C_{34} homohopane 22S/(22S + 22R)	0.36	0.33	0.51
C_{33} homohopane 22S/(22S + 22R)	0.72	0.81	0.37
C_{32} homohopane 22S/(22S + 22R)	0.29	0.27	0.45
C_{31} homohopane 22S/(22S + 22R)	0.37	0.30	0.49
C_{31-35} homohopanes 22S/(22S + 22R)	0.41	0.42	0.47
C_{29}T/(C_{29} hopane + C_{29}T)	0.12	0.05	0.20
Ts/(Ts + Tm)	0.09	0.06	0.37
Moretane/hopane ratios	0.37	0.35	0.24
ßα/(αß + ßα) C_{29} hopane	0.41	0.40	0.27
ßα/(αß + ßα) C_{30} hopane	0.27	0.26	0.20
ßα/(αß + ßα) C_{31} hopane	0.44	0.46	0.20
Hopanes/steranes	1.49	0.92	0.86
2-Methylhopane index (C_{31}MHI)	0.65%	0.31%	0.27%
2-Methylhopane index (C_{32}MHI)	1.79%	1.00%	0.27%
C_{32} 2- Methylhopane 22S/(22S+22R)	0.59	0.61	0.56
C_{33} 2- Methylhopane 22S/(22S+23R)	0.65	0.54	0.54
C_{34} 2- Methylhopane 22S/(22S+24R)	0.59	0.65	0.58
C_{35} 2- Methylhopane 22S/(22S+25R)	0.58	0.63	0.53
C_{36} 2- Methylhopane 22S/(22S+26R)	0.66	0.67	0.51

bacteria can produce their precursors. The relative content of 2-methylhopane in concretions was 2.4–6.6 times that in mudstones (C_{31}MHI: 0.65% *vs.* 0.27%; C_{31}MHI: 1.79% *v.* 0.27%), pointing to a higher concentration of microorganisms in the concretions.

In some research on carbonate concretions (Mavotchy et al., 2016; Lengger et al., 2017), the ^{13}C isotope in the organic matter of concretions was generally found to be 1‰–2‰ lighter than that in surrounding rocks (Plet et al., 2016). This is probably due to the presence of other organic matter that consumes ^{13}C in the concretions, such as methane-oxidizing bacteria and sulfate-reducing bacteria. However, an opposite trend was detected in this study. This is probably because the influence exerted by the weathering of surrounding rocks on isotopes of individual N-alkane hydrocarbons exceeded that of bacteria-induced biochemical action in the concretions.

Based on the above analysis, we infer that carbonate concretions can better preserve molecular fossils. Compared with the

surrounding rock, they have three major advantages. ① The thermal evolution degree of the organic matter in the concretions is lower than that in the host rock. Thus, a more primitive biomolecular composition can be retained. ② The geochemical characteristics of shales near the surface are affected by external fluids, while the concretions can resist any interference by external fluids. As a result, the molecular fossils inside them remain unaffected. ③ In outcrop areas without drilling, shales are often eroded, so that concretions with molecular fossil information can be well preserved to provide valuable paleontological records, and biomarker analysis can be used to determine their origin.

That being said, the concretion samples in this study were collected from the same stratum outcrop. In terms of basin scale, it is necessary to study more samples to support whether carbonate nodules of different ages have similar characteristics.

7 Conclusion

There are obvious geochemical differences inside and outside the concretions. During the sedimentation of shales, most biomarkers are preserved in concretions. Comparative research on biomarkers indicates that compared with those in shales, the molecular fossils in concretions have a lower degree of evolution and are subject to weaker catalysis and weathering action. Hence, their organic molecules are better preserved. Therefore, concretions and the organic matter preserved therein are of great significance for acquiring information on paleontological lipids and gaining new insights into early life.

This study dissected two groups of concretion and surrounding rock samples, which show similar characteristics in most analyses and tests. However, there are discrepancies between the concretions and shales due to multiple factors, including chronology, paleoenvironment, mineral composition, and microbial degradation. In-depth organic geochemical research on carbonate concretions in shales is thus important. In future work, multidisciplinary techniques and methods should be integrated to identify the ancient microbial ecosystems in concretions, which may provide new insights for early life research.

Data availability statement

The original contributions presented in the study are included in the article/Supplementary Material, further inquiries can be directed to the corresponding author.

Author contributions

Methodology, LL and FC; validation, JX; investigation, LL; data curation, FC and JX; writing—original draft preparation, LL; writing—review and editing, LL, FC and JX; project administration, LL. All authors have read and agreed to the published version of the manuscript.

Funding

This work was supported by the National Nature Science Foundation of China (41902128). The authors gratefully acknowledge the financial support.

Conflict of interest

The authors declare that the research was conducted in the absence of any commercial or financial relationships that could be construed as a potential conflict of interest.

Publisher's note

All claims expressed in this article are solely those of the authors and do not necessarily represent those of their affiliated organizations, or those of the publisher, the editors and the reviewers. Any product that may be evaluated in this article, or claim that may be made by its manufacturer, is not guaranteed or endorsed by the publisher.

References

Abdel-Wahab, A., and Mcbride, E. F. (2001). Origin of giant calcite-cemented concretions, temple member, qasr el sagha formation (eocene), faiyum depression. *Egypt. J. Sediment. Res.* 71, 70. doi:10.1306/031700710070

Abedini, A., and Calagri, A. A. (2017). Geochemistry of claystones of the Ruteh Formation, NW Iran: Implications for provenance, source-area weathering, and paleo-redox conditions. *njma.* 194, 107–123. doi:10.1127/njma/2017/0040

Abedini, A., and Khosravi, M. (2022). Geochemical constraints on the Zola-Chay river sediments, NW Iran: Implications for provenance and source-area weathering. *Arab. J. Geosci.* 15, 1515–1517. doi:10.1007/s12517-022-10822-y

Abedini, A., Rezaei Azizi, M., and Calagari, A. A. (2018). Lanthanide tetrad effect in limestone: A tool to environment analysis of the ruteh formation, NW Iran. *Acta Geodyn. Geomater.* 15, 229–246. doi:10.13168/agg.2018.0017

Abedini, A., Rezaei Azizi, M., and Dill, H. G. (2020). formation mechanisms of lanthanide tetrad effect in limestones: An example from arbanos district, NW Iran. *Carbonates Evaporites* 35, 1–18. doi:10.1007/s13146-019-00533-z

Clifton, H. E. (1957). The carbonate concretions of the Ohio shale. *Ohio J. Sci.* 57 (2), 114–124. Available at: http://hdl.handle.net/1811/4432.

Coleman, M. L. (1993). Microbial processes: Controls on the shape and composition of carbonate concretions. *Mar. Geol.* 113, 127–140. doi:10.1016/0025-3227(93)90154-N

Dale, A., John, C. M., Mozley, P. S., Smalley, P. C., and Muggeridge, A. H. (2014). Time-capsule concretions: Unlocking burial diagenetic processes in the mancos shale using carbonate clumped isotopes. *Earth Planet. Sci. Lett.* 394, 30–37. doi:10.1016/j.epsl.2014.03.004

Das, S. S., and Tripathi, M. K. (2009). Trace fossils from Talchir carbonate concretions, Giridih basin, Jharkhand. *J. Earth Syst. Sci.* 118, 89–100. doi:10.1007/s12040-009-0009-6

Dong, J., Hu, Z. W., Yuan, X. Q., He, J., Li, Y., and Wang, Y. L. (2017). The carbonate concretions of Chang-7 and their hydrocarbon significance in southern Ordos Basin, China. *J. Chengdu Univ. Technol.* 44 (5), 555–564. doi:10.3969/j.issn.1671-9727.2017.05.06

Hudson, J. D., Coleman, M. L., Barreiro, B. A., and Hollingworth, N. T. J. (2001). Septarian concretions from the oxford clay (jurassic, england, UK): Involvement of original marine and multiple external pore fluids. *Sedimentology* 48, 507–531. doi:10.1046/j.1365-3091.2001.00374.x

Jin, R. G. (1989). A deep water sedimentary criteria-"Knotty nodule" and origin. *Acta Sedimentol. Sin.* 7 (2), 51–58.

Khokhlova, O., Myakshina, T., and Kuznetsova, A. (2021). Origins of hard carbonate nodules in arable Chernozems in the Central Russian Upland. *Eur. J. Soil Sci.* 72, 326. doi:10.1111/ejss.12948

Lash, G. G. (2015). Authigenic barite nodules and carbonate concretions in the Upper Devonian shale succession of Western NewYork- A record of variable methane flux during burial. *Mar. Pet. Geol.* 59, 305–319. doi:10.1016/j.marpetgeo.2014.09.009

Lash, G. G., and Blood, D. (2004). Geochemical and textural evidence for early (shallow) diagenetic growth of stratigraphically confined carbonate concretions, Upper Devonian Rhinestreet Black Shale, Western New York. *Chem. Geol.* 206, 407–424. doi:10.1016/j.chemgeo.2003.12.017

Lengger, S. K., Melendez, I. M., Summons, R. E., and Grice, K. (2017). Mudstones and embedded concretions show differences in lithology-related, but not source-related biomarker distributions. *Org. Geochem.* 113, 67–74. doi:10.1016/j.orggeochem.2017.08.003

Lin, L. M., Liu, S., Xu, Y., and Li, F. L. (2021). Lithofacies and pore structure of fine-grained sedimentary rocks of Qing-1 Member of Cretaceous in the southern Songliao basin. *Acta Geol. sinica-. Engl. Ed.* 95 (2), 570–584. doi:10.1111/1755-6724.14657

Liu, B., Liu, Y., Liu, Y., He, J. L., Gao, Y. F., Wang, H. L., et al. (2020). Prediction of low-maturity shale oil produced by *in situ* conversion: A case study of the first and second members of Nenjiang Formation in the central depression, southern Songliao Basin, northeast China. *Pet. Geol. e.* 42 (4), 533–544. doi:10.11781/sysydz202004533

Liu, Y. C., Liu, B., Cheng, L. J., Xing, J. L., Tian, S. S., Huang, S. P., et al. (2021). Modeling of tectonic-thermal evolution of cretaceous qingshankou shale in the changling sag, southern Songliao Basin, NE China. *Front. Earth Sci. (Lausanne).* 9, 694906. doi:10.3389/feart.2021.694906

Luo, X., Wang, H., Zhang, Z., Liu, W., Wang, X., and Zhang, Z. S. (2020). Carbon and oxygen isotopes of calcified root cells, carbonate nodules and total inorganic carbon in the Chinese loess–paleosol sequence: The application of paleoenvironmental studies. *J. Asian Earth Sci.* 201, 104515. doi:10.1016/j.jseaes.2020.104515

Mavotchy, N. O., El Albani, A., Trentesaux, A., Fontaine, C., Pierson-Wickmann, A. C., Boulvais, P., et al. (2016). The role of the early diagenetic dolomitic concretions in the preservation of the 2.1Ga paleoenvironmental signal: The Paleoproterozoic of the Franceville Basin, Gabon. *Comptes Rendus Geosci.* 348, 609–618. doi:10.1016/j.crte.2016.08.002

Melendez, I., Grice, K., Trinajstic, K., Ladjavardi, M., Greenwood, P., and Thompson, K. (2013). Biomarkers reveal the role of photic zone euxinia in exceptional fossil preservation: An organic geochemical perspective. *Geology* 41, 123–126. doi:10.1130/G33492.1

Mojarro, A., Cui, X. Q., Zhang, X. W., Jost, A. B., Bergmann, K. D., Vinther, J., et al. (2022). Comparative soft-tissue preservation in Holocene-age capelin concretions. *Geobiology* 20, 377–398. doi:10.1111/gbi.12480

Nabbefeld, B., Grice, K., Twitchett, R. J., Summons, R. E., Hays, L., Bottcher, M. E., et al. (2010). An integrated biomarker, isotopic and palaeoenvironmental study through the Late Permian event at Lusitaniadalen, Spitsbergen. *Earth Planet. Sci. Lett.* 291 (1-4), 84–96. doi:10.1016/j.epsl.2009.12.053

Ou, L. H., Yi, H. S., Xia, G. Q., Qian, L. J., Qiu, Y. B., and Zhang, C.(2013). Origin and petroleum geological significance of carbonate rock concrete in Linxi Formation, northeast of Inner Mongolia, China. *J. Chengdu Univ. Technol.* 40(4), 438–443. doi:10.3969/j.issn.1671-9727.2013.04.12

Plet, C., Grice, K., Pages, A., Ruebsam, W., Coolen, M. J. L., and Schwark, L. (2016). Microbially-mediated fossil-bearing carbonate concretions and their significance for palaeoenvironmental reconstructions: A multi-proxy organic and inorganic geochemical appraisal. *Chem. Geol.* 426, 95–108. doi:10.1016/j.chemgeo.2016.01.026

Rabassa, J. (2006). Unusual morphology of calcareous concretions in glaciolacustrine sediments, late Pleistocene, Lago Ghio, Patagonia, Argentina-A short note. *Quat. Int.* 147, 113–115. doi:10.1016/j.quaint.2005.11.001

Railsback, L. B. (2021). Pedogenic carbonate nodules from a forested region of humid climate in central Tennessee, USA, and their implications for interpretation of C3-C4 relationships and seasonality of meteoric precipitation from carbon isotope (δ13C) data. *Catena* 200, 105169. doi:10.1016/j.catena.2021.105169

Raiswell, R., and Fisher, Q. J. (2000). Mudrock-hosted carbonate concretions: A review of growth mechanisms and their influence on chemical and isotopic composition. *J. Geol. Soc. Lond.* 157, 239–251. Available at: https://pubs.geoscienceworld.org/jgs/article/157/1/239/320041/Mudrock-hosted-carbonate-concretions-a-review-of?doi=10.1144%2fjgs.157.1.239.

Rowley, D. B., and Currie, B. S. (2006). Palaeo-altimetry of the late eocene to miocene lunpola basin, central tibet. *Nature* 439 (7077), 677–681. doi:10.1038/nature04506

Schopf, J. W., Kudrayavtsev, A. B., Agresti, D. G., Wdowiak, T. J., and Czaja, A. D. (2002). Laser-Raman imagery of Earth's earliest fossils. *Nature* 416, 73–76. doi:10.1038/416073a

Schopf, J. W. (1993). Microfossils of the early archean apex chert: New evidence of the antiquity of life. *Science* 260, 640–646. doi:10.1126/science.260.5108.640

Scotchman, I. C., Carr, A. D., and Astin, T. R. (2000). Porefluid evolution in the kimmeridge clay formation of the UK outer moray firth. *J. Geochem. Explor.* 69-70, 53–57. doi:10.1016/S0375-6742(00)00044-3

Sun, Y., Li, Y., Li, K., Li, L., and He, H. P. (2021). Massive deposition of carbonate nodules in the hyperarid northwest Qaidam Basin of the northern Tibetan Plateau. *Geochem. Geophys. Geosyst.* 22 (4), 1–10. doi:10.1029/2021GC009654

Sun, Y., Zhong, J. H., Jiang, Z. X., Yu, W. Q., Cao, Y. C., and Rao, M. Y. (2006). Study of sequence stratigraphy of depression period in southern Songliao Basin. *J.China U. Pet.* 30 (5), 1–7.

Taylor, Y., and McLennan, S. M. (1985). *The continental crust: Its composition and evolution*. 1st edn. Oxford: Blackwell.

Tazaki, K., and Morii, I. (2008). Microbial immobilization of Si, Mn, Fe, and Sr ions in the nacreous layer of sinohyliopsis schlegeli and environmental factors. *Earth Sci. Front.* 15 (6), 54–65. doi:10.1016/S1872-5791(09)60008-7

Wakeham, S. G., Hopmans, E. C., Schouten, S., and Damste, J. S. S. (2004). Archaeal lipids and anaerobic oxidation of methane in euxinic water columns: A comparative study of the black sea and cariaco basin. *Chem. Geol.* 205, 427–442. doi:10.1016/j.chemgeo.2003.12.024

Wanas, H. A. (2008). Calcite-cemented concretions in shallow marine and fluvial sandstones of the birket qarun formation (late eocene), el-faiyum depression, Egypt: Field, petrographic and geochemical studies: Implications for formation conditions. *Sediment. Geol.* 212, 40–48. doi:10.1016/j.sedgeo.2008.09.003

Wang, L., Cao, X. X., Li, Y., Yin, Q., and Song, Z. G. (2015). The carbon isotopic composition of individual biomarkers in lacustrine source rocks from Songliao Basin and its biogeochemical implication. *Geochimica* 44 (4), 337–347. doi:10.19700/j.0379-1726.2015.04.003

Woo, K. S., and Khim, B. K. (2006). Stable oxygen and carbon isotopes of carbonate concretions of the Miocene Yeonil Group in the Pohang Basin, Korea: Types of concretions and formation condition. *Sediment. Geol.* 183, 15–30. doi:10.1016/j.sedgeo.2005.09.005

Wu, Y. K., Luo, S. M., Wang, D. F., Burns, S. J., Li, E., DeGroot, D. J., et al. (2021). Origin, growth, and characteristics of calcareous concretions in the varved sediments of a Glacial Lake. *Eng. Geol.* 287, 106112–106118. doi:10.1016/j.enggeo.2021.106112

Xu, W., Yang, G. Q., Li, A., Song, Z. X., and Hu, W. H. (2022). Determination of favorable lithofacies for continental shale gas: A case study of the shahezi formation, changling fault depression, Songliao Basin. *Front. Earth Sci. (Lausanne).* 10, 916326. doi:10.3389/feart.2022.916326

Yang, S. Y., Schulz, H. M., Horsfield, B., Schovsbo, N. H., Grice, K., and Zhang, J. C. (2020). Geological alteration of organic macromolecules by irradiation: Implication for organic matter occurrence on Mars. *Geology* 48 (7), 713–717. doi:10.1130/G47171.1

Yemane, K., and Kelts, K. (1996). Isotope geochemistry of Upper Permian early diagenetic calcite concretions: Implications for Late Permian waters and surface temperatures in continental Gondwana. *Palaeogeogr. Palaeoclimatol. Palaeoecol.* 125, 51–73. doi:10.1016/S0031-0182(96)00024-7

Zhang, Q., Zhang, Y. X., Wang, B. H., Yin, S., Wu, X. S., and Yuan, C. S. (2022). Comprehensive evaluation and reservoir classification in the quan 3 member of the cretaceous quantou Formation in the fuxin uplift, Songliao Basin. *Front. Earth Sci. (Lausanne).* 10, 1016924. doi:10.3389/feart.2022.1016924